Interaction control capabilities of an MR-compatible compliant actuator for wrist sensorimotor protocols during fMRI

Fabrizio Sergi, *Member, IEEE,* Andrew C. Erwin *Student Member, IEEE,* and Marcia K. O'Malley *Senior Member, IEEE*

***Abstract*— This paper describes the mechatronic design and characterization of a novel MR-compatible actuation system designed for a parallel force-feedback exoskeleton for measurement and/or assistance of wrist pointing movements during functional neuroimaging. The developed actuator is based on the interposition of custom compliant elements in series between a non-backdrivable MR-compatible ultrasonic piezoelectric motor and the actuator output. The inclusion of physical compliance allows estimation of interaction force, enabling force-feedback control and stable rendering of a wide range of haptic environments during continuous scanning. Through accurate inner-loop velocity compensation and force-feedback control, the actuator is capable of displaying both a low-impedance, *subject-in-charge* mode, and a high stiffness mode. These modes enable the execution of shared haptic protocols during continuous fMRI.**

The detailed experimental characterization of the actuation system is presented, including a backdrivability analysis, demonstrating an achievable impedance range of 22 dB, within a bandwidth of 4 Hz (for low stiffness). The stiffness control bandwidth depends on the specific value of stiffness: a bandwidth of 4 Hz is achieved at low stiffness (10% of the physical springs stiffness), while 8 Hz is demonstrated at higher stiffness. Moreover, coupled stability is demonstrated also for stiffness values substantially (25%) higher than the physical stiffness of the spring. Finally, compatibility tests conducted in a 3T scanner are presented, validating the potential of inclusion of the actuator in an exoskeleton system for support of wrist movements during continuous MR scanning, without significant reduction in image quality.

***Index Terms*— functional MRI (fMRI), MR-compatible robotics, force control, compliant actuators.**

I. INTRODUCTION

Robot-aided rehabilitation has been successfully demonstrated to introduce standardization and repeatability to movement rehabilitation techniques, paving the way for the implementation of novel and neuroscience-based rehabilitation protocols. However, it is not yet clear which control modes are capable of promoting more functional or faster recovery. Although it is generally accepted that therapies based on continuous passive motion do not contribute to recovery in chronic stroke [1], the definition of an "optimal" therapy for a given subject or subject group is far from realization. It is indeed agreed that a deeper understanding of the neural correlates of movement therapy after neurological injury is necessary for the development of more effective rehabilitation training programs [2]. Neuroimaging techniques such as fMRI (functional Magnetic Resonance Imaging) can shed light on such processes, representing an appealing opportunity to study the treatment-effect relationship of robot-aided neurorecovery. Unfortunately, the same level of standardization and reproducibility of motor protocols recently obtained through robots for the therapy (treatment delivery) phase is far from having been achieved in motor protocols in MRI environments (effect measurement).

The requirement for MR compatibility does indeed pose strong technological challenges to the introduction of robotic devices to measure and/or assist human movements during scanning. The structural materials most often used in conventional robotic and mechatronic systems for the desired mechanical properties such as strength, rigidity, and machinability often have high magnetic susceptibility [3], [4]. Most importantly, MR-compatible robots have to address the lack of suitable off-the-shelf actuation and sensing technologies. Commonly used electromagnetic actuators are intrinsically not MR-compatible due to their principle of operation. Efforts have been recently devoted to the integration of mechanical supports and electromagnetic shielding that enable operation of low-impedance DC motors for motor protocols during continuous fMRI [5]. However, these solutions require the transfer of mechanical power through fairly long rods, with a possible accuracy degradation, especially at high frequencies. Fluidic actuation is instead intrinsically MR-compatible: hydraulic power can be transferred through long hoses, enabling remote placement of the power source and power distribution components [6]. This actuation scheme is affected by high friction and by the limited dependability achievable in an environment that cannot be fully structured for continuous use with a hydraulic robot, as is the case of MRI scanners. Pneumatic systems are mainly suitable for relatively low-force applications, and they have limited stiffness range and force regulation bandwidth [7]. Non-conventional actuation systems such as electrorheological fluids (ERFs) are an alternative way for generating resistive forces [8] or actuation forces [9] in MR environments. Among the systems developed so far, a promising actuation approach is represented by UltraSonic Motors (USMs), featuring intrinsic magnetic immunity, bidirectionality, high torque-to-weight ratio, small size, and compact shape [4], [10]. Although USMs have been successfully used in surgical robotics applications [4], [11], their extension to sensorimotor protocols is hindered by USMs' high intrinsic impedance, which prohibits the implementation of "direct interaction control," as defined in [12], which requires force-sourced actuators with minimal intrinsic impedance.

Other issues arise from experimental conditions that limit the application of motor protocols during fMRI. Most of the previous studies with relevance to motor control and/or motor rehabilitation involve shoulder and/or elbow movements [13]–[16], and it is well known that fMRI is very sensitive to head movements and to magnetic field changes introduced by movement of body parts occurring near the scanning site [17]. Both factors can potentially lead to motion artifacts inducing false-positive activity or masking actual brain activation. Therefore, in order to determine correct functional activation maps during motor tasks, it becomes crucial to attenuate these motion artifacts. A significant amount of research has been devoted to correcting the issues of head movements during scanning, through rigid body image realignment, the use of a bite bar to minimize head movements, offline analysis of variance with downweighting of motion-corrupted images, or model-based attenuation of movements artifacts [18].

In this research, we aim to look at movements of more distal joints of the upper arm. Such movements involve activation of a wide motor cortex area, and movement of less body mass in a region that is farther from the region-of-interest (ROI), likely generating a reduced amount of motion artifacts. However, assistance and measurement of movements of the distal degree of freedoms such as the wrist joint are challenging from a robot design standpoint, since they require accurate force control and minimal dynamical perturbation to subjects' movements.

This paper presents the design of a novel MR-compatible wrist robot, the MR-RiceWrist, and the validation of its primary subsystem: a custom-developed compliant actuator (MR-SEA) with capabilities for accurate interaction control. The proposed architecture is the paraphrasis of the Series Elastic Actuator (SEA) concept [19] to the specific needs of interaction control in motor protocols for fMRI, consisting of the interposition of a compliant force-sensing element in series between a MR-compatible and non-backdrivable actuator and the output. The proposed solution enables implementation of force-feedback control with non-backdrivable actuators through the measurement of macroscopic deflections of the compliant elements. These measurements can be obtained via sensors commercially available in MR-compatible versions, such as optical encoders with proper RF filtering. Interaction control capabilities of the MR-SEA are demonstrated through experiments conducted in a 1-DOF test bench that assess its performance for both the zero-force mode and for a wide range of virtual stiffness values, including higher stiffness than the physical compliance of the actuator. A detailed analysis of MR-compatibility is conducted to demonstrate that the system can be continuously operated during scanning without significantly compromising image quality.

II. MR-RiceWrist design

We present the design of a robot that can simultaneously measure, assist and perturb movements of the two most distal degrees of freedoms of wrist pointing movements, i.e. flexion/extension (FE) and radial/ulnar deviation (RUD), when a subject is asked to conduct visually-guided movements during fMRI.

A. Analysis of specifications

Ideally, the wrist robot should be compatible with human wrist rotations, whose range can be as high as 115 deg for FE and 70 deg for RUD for activities of daily living (ADL) [20]. However, this is currently a utopian requirement, given the limitations of fMRI, deriving from both scanner space constraints and by the need of minimizing head movements and magnetic field distortion. Under this consideration, we confine our design to a circular region with radius ± 20 deg in the end-effector plane (comprising FE joint rotation and RU joint rotation) for both degrees of freedom. As far as actuation requirements, we derive from biomechanical analyses of ADL [20] that wrist actuation torques are modest, with a maximum of 0.35 Nm required for both FE and RU. Extending the domain of applicability of the wrist robot to motor perturbations studies, we set as a design requirement a minimum torque of 1.5 Nm, in accordance with torque capabilities of wrist exoskeletons used for rehabilitation [21]–[23].

To enable operation in a *transparent* mode during interaction with subjects, we seek to minimize the force required to back-drive the system. To define a design specification on the backdrivability of the system, we consider the uncompensated friction properties of low-impedance robots used for wrist robotic therapy [22], [24], [25] and for biomechanics or motor control studies [26], [27]. An average static friction of 0.06 Nm is reported in [22], while our recently developed RiceWrist-S [25] results in a maximum static friction of 0.2 Nm for both DOFs). In the wrist robots described above, the achieved zero-force dynamic range[1] (defined as the ratio between the maximum value of force that can be displayed to the subject and the minimum force required to back-drive the robot in the minimum impedance mode) ranges between 20 and 30 dB.

B. Conceptual design

Through measurements on a 700 mm bore diameter, 3T MR scanner available at the Methodist Hospital Research Institute (Philips Ingenia), we measured the distance along the scanner axis between the scanner isocenter and the edge of the cylindrical scanner to be approximately 750 mm. In those conditions, during fMRI, the wrist of a normal-sized subject laying in the conventional supine position during scanning, with the elbow moderately flexed and supported by an angled base, would be approximately situated at the edge of the scanner. An exoskeletal design would require the presence of robotic parts worn at the forearm, which be located inside the scanner bore during scanning. Given the limited space available in the scanner, and considering the pressing need of minimizing the probability of collision of robotic parts with the scanner bore, we pursue an end-effector robot design, with the robot handle as the single point of interaction.

We then chose to pursue a parallel 3RPS kinematics scheme, for the increased structural stiffness compared to serial robots, for the opportunity of replicating the same structure of the RiceWrist [21] used for rehabilitation therapy, and, finally, for the possibility of placement of actuators farther from the ROI. The handle orientation is then reversed relative to the RiceWrist exoskeleton, resulting in a end-effector type design (see Fig. 1).

[1] A force-related measure is considered, instead of the more conventional impedance dynamic range used in haptics, because the dynamics of these systems, especially at the low speeds involved during rehabilitation therapy, are dominated by static friction, hence exhibiting mostly velocity-independent backdrivability forces

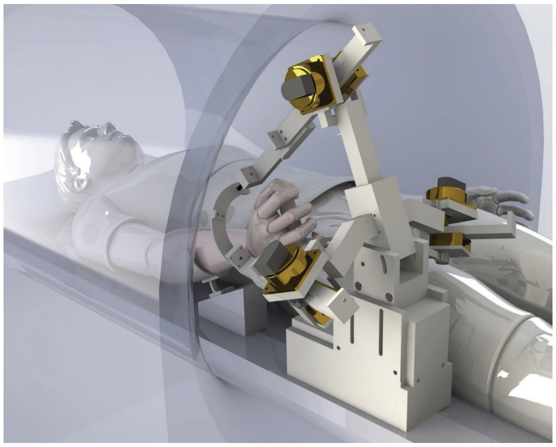

Fig. 1. 3D rendering of the MR-compatible wrist robot, including the actuators presented in this paper.

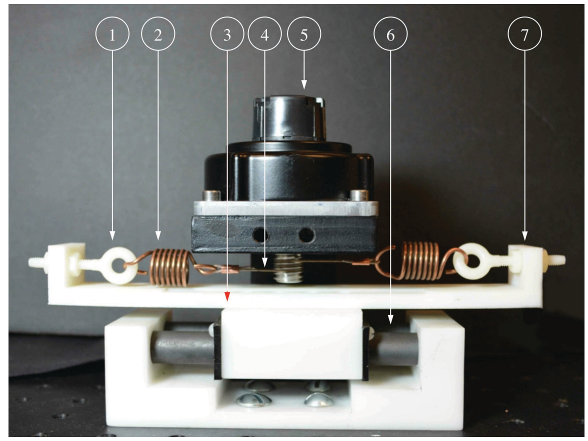

Fig. 2. Lateral view of the developed prototype. (1) Nylon eyebolts for springs pretension, (2) extension springs, (3) slider, (4) cable transmission, (5) USM motor with rotary encoder, (6) molded carbon graphite shafts, (7) carriage. The linear encoder that measures the linear displacement of the carriage is not visible in this picture, to facilitate visualization of the cable transmission.

Given this manipulator selection, the requirements for the three linear actuators are a maximum continuous force of 20 N (resulting in a maximum torque of 2 Nm) and a resistance force of less than 1 N in zero-force mode, with a maximum operating velocity of 100 mm/s. Among others, motors suitable for this application are piezoelectric actuators, that are based on a non-magnetic actuation principle. Given the high intrinsic impedance of piezoelectric actuation, a force-feedback control scheme is adopted, to regulate interaction during subject-in-charge interaction modes.

C. Actuator design

The SEA solution has been chosen to satisfy the specifications reported above, because it is capable of providing an accurate and low-impedance force source using a non-backdrivable MR-compatible actuator in conjunction with compliant elements. Both key elements of the actuation architecture, the motor and the compliant elements, can be easily made of non-magnetic and low-conductivity materials. The developed prototype (MR-SEA) includes the following components: a rotary ultrasonic piezoelectric motor (60W Shinsei USR60-E3N)[2]; a threaded pulley on the motor shaft, a cable transmission (braided fishing line - 0.4 mm diameter Teflon-coated polyethylene cables)[3]; custom-designed phosphor bronze extension springs (stiffness: 1.9±10% N/mm[4], max force: 36 N); a custom-designed Delrin carriage; a custom-designed linear bearing, supporting the carriage[5].

The cable is wrapped around the shaft-mounted pulley, and connected at its two extremities to the extension springs. A locking mechanism composed of plastic eyebolts and locking nuts is used to pretension the extension springs to a value that corresponds roughly to half of their maximum force/displacement range. The preloaded springs are then connected to the carriage, supported by the custom designed linear bearing, composed of two parallel molded carbon graphite rods, that support two precision borosilicate glass (Pyrex) tubes, included in through holes in the slider. Physical compliance, resulting from the parallel connection of the two springs, is thereby connected in series between the actuator and the load, thus forming the SEA architecture. The motor is shipped with an optical incremental encoder (1000 pulses per revolution) that results in a 0.09 deg quantization in the measurement of motor rotation (0.01 mm in the measurement of the cable displacement). Load displacement is measured through a linear optical encoder system, composed of a 500 lines-per-inch optical strip fixed on the slider and a stationary reading head[6].

This arrangement of compliant elements has been conceived in order to minimize the number of bearings in the system. In fact, MR-compatible bearings are relatively more expensive compared to standard solutions that do not have to satisfy the MR-compatibility requirement. In contrast to most existing linear SEA designs, the proposed solution does not require the introduction of additional bearings, compared to the non-compliant actuator solution. Table I describes the details of the components employed in the MR-SEA.

III. Actuator modeling and control

The basic mechanical model for a Series Elastic Actuator is presented in Fig. 3(a). It includes a motor, that applies a force F_M driving the output mass through a spring/mass/damper system. The basic differential equation for this system is:

$$m_M \ddot{x}_M + b_M \dot{x}_M = F_M - F_S = F_M - k_S(x_M - x_L), \tag{1}$$

with x_M and x_L representing motor and load displacements, respectively, m_M the reflected inertia of the motor, b_M is the linear coefficient of viscous friction of the geared motor seen

[2]Manufactured and sold with the velocity controller by Shinsei Corporation, Tokyo, Japan

[3]Commercial name: *Spiderwire Stealth*, Spiderwire, Columbia, SC, USA

[4]Manufactured by Spring Engineers of Houston Ltd., Houston, TX, USA

[5]Carbon graphite shafts manufactured by Ohio Carbon Blank Inc., Willoughby, OH, USA, Pyrex tubes manufactured by Wilmad LabGlass, Buena, NJ, USA

[6]LIN-500 and EM1-0-500-I, US Digital Corporation, Vancouver, WA, USA

TABLE I

MATERIALS USED IN THE MR-SEA PROTOTYPE - χ VOLUME SUSCEPTIBILITY, σ ELECTRICAL CONDUCTIVITY

Component	Material	χ [ppm]	σ [% IACS]
Ultrasonic motor shaft and springs	Phosphor bronze UNS C54400	-52	18.49
Cable	Teflon-coated polyethylene	2	$< 10^{-11}$
Bearings shafts	Molded carbon graphite	-9	$< 10^{-5}$
Bearings sliding parts	Borosilicate glass	-16.3	$< 10^{-13}$
Slider, supporting parts, fasteners	Delrin - nylon	$\lvert\chi\rvert <5$	$< 10^{-13}$
High-stress screws	Brass C36000	112	25.3

at the spring port, k_S the linear spring stiffness and F_S the force of interaction between the actuator and the environment.

Several control approaches have been proposed for force control of SEAs, including direct force feedback controllers with linear feedforward compensation terms [28], nonlinear compensators to reduce the effects of friction and variability of interaction dynamics [29] and the application of cascaded linear force-position [30] or force-velocity control [31], [32]. Among the mentioned controllers, the last two approaches are particularly interesting, since they allow the conversion of a force control problem into simpler position or velocity control problems. Also, through such controllers, it is possible to implement interaction controllers in highly non-transparent actuators, without requiring a detailed knowledge of system parameters. Moreover, the cascaded force and velocity control scheme is passive [32], for a wide set of controller gains. The motor is shipped with a factory-tuned velocity control box, that regulates motor velocity through 10 m long power lines, enabling placement of the controller outside the scanning room. Due to the controller inherent robustness to transmission nonlinearities, the cascaded force-velocity control scheme was selected for this work.

This control scheme can be simplified using linear systems theory. To this aim, the inner velocity loop can be modeled by the superposition of two contributions, one describing velocity control performance, and the other one describing the degradation of velocity control due to the interaction with the environment:

$$V_M(s) = H_V(s)V_{des}(s) + D_V(s)F_S(s), \tag{2}$$

where H_V is the velocity control closed loop transfer function, in the absence of torque disturbance ($H_V = C_V G/(1 + C_V G)$), D_V describes the effect of torque disturbance on velocity control output ($D_V = -G/(1 + G_V G)$), and G is the plant subject to velocity control, a mass-damper system ($G = 1/(m_M s + b_M)$). The simplified block diagram in the Laplace domain is shown in Fig. 3(c).

The next section will report on system identification conducted to estimate the transfer functions $H_V(s)$ and $D_V(s)$, that will be subsequently used for control design, simulation and testing of the controlled motor.

A. System identification of the velocity-controlled motor

1) Unperturbed motor case: To estimate the transfer function $H_V(s)$, a voltage command was fed to the USM motor velocity controller, and the resulting velocity was calculated offline through a third order Savitzky-Golay filter, with a window size of 11 samples (10 ms). A first experiment was conducted to calculate the static mapping between commanded voltage and velocity, by applying 0.1 V step-wise increases in voltage in the range (0-3.33 V) and measuring the resulting velocity through averaging in a 3-s window, after the velocity transient ceased (0.5 s). The resulting static calibration curve of the velocity-controlled actuator, shown in Fig. 4, includes the low-amplitude dead-band zone and the high-amplitude saturation zone. Within the linear region, the measured velocity ω, expressed in rpm, is linear with the applied voltage v ($\omega = 49.25v - 6.62$, $R^2 = 0.999$), with a maximum linearity error lower than 1% of the value predicted by linear regression, in all cases.

Dynamic experiments were later conducted, with voltage applied as a symmetric Schroeder multisine profile, with variable peak value amplitude and flat frequency spectrum in the range (0.01-20) Hz. Through measurement of the resulting velocity, the H_V transfer function was estimated through a parametric transfer function consisting of two underdamped poles and one zero, using the MATLAB function `pem`, whose Bode plot is shown in Fig. 5(a), that shows that higher amplitude responses have overshoot up to 3 dB in a frequency above 1 Hz, until higher modes are excited.

In the case of the inner velocity loop of a SEA controlled through a cascaded force-velocity action, the presence of overshoot results in the limited capability to set the proportional force gain, if passivity is desired, as shown in Fig. 5(b). To avoid this problem and guarantee the possibility of stable rendering of a wide range of impedance through the cascaded force-velocity control, a feedforward non-linear inner loop compensation scheme has been developed. The compensation scheme is based on the following steps: *i)* inversion of the estimated $H_V(s)$ transfer function, for the discrete set of desired velocity values shown in Fig. 5(a)[7]; *ii)* approximation of the set of resulting compensators to a family of compensators $C_\zeta = \frac{1+T_z s}{1+(2\zeta T_w)s+(T_w s)^2}$, with constant T_z and T_w, and ζ, defined by the linear mapping between the low-velocity condition $\omega_{des} \leq 50$ rpm, and the high-velocity condition $\omega_{des} \geq 100$ rpm - Fig. 5(c); *iii)* use of an amplitude dependent compensation scheme, obtained by linear combination of the two compensators tuned high- and low-velocity conditions, using the scheme visually represented in Fig. 5(d). To characterize the performance of the resulting non-linear velocity compensation

[7]This step required the addition of one high-frequency pole to the resulting anti-causal compensator.

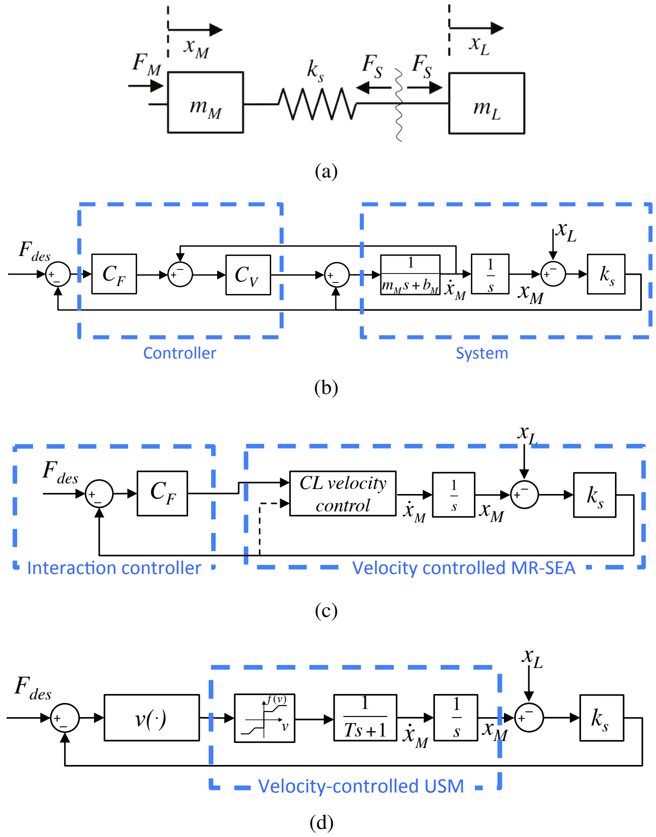

Fig. 3. Analysis and simplification of MR-SEA force control. (a) Schematic of a Series Elastic Actuator. A motor is connected to the load through a spring, whose deflection is measured, thus allowing the measurement of the interaction force F_S. (b) Linear block diagram in the mechanical domain of a SEA subject to a cascaded force-velocity control. (c) Block diagram of the proposed controller for the MR-SEA. A non-backdrivable motor is controlled to be a velocity source, and an outer loop is closed on the measured force of interaction with the environment. A velocity control disturbance transfer function can be defined to describe the effect of interaction force on the velocity control error. (d) Block diagram used for simulations in [33] and for the experimental section in this paper. The velocity-controlled motor is modeled as the series of a saturation block, a low-amplitude dead-band and a low-pass filter.

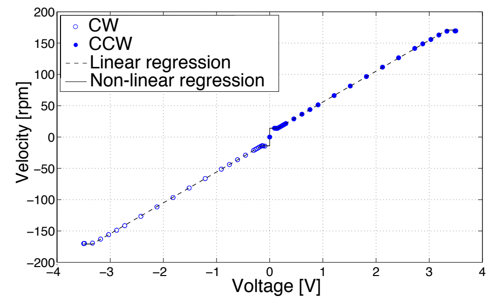

Fig. 4. Static calibration curve of the velocity-controlled motor. Linear regression is conducted in the range (0.15-3.33) V. The linearity error resulting in this range is less than 1% of the commanded value in all cases. The minimum velocity that can be regulated through the factory-supplied velocity controller is 14 rpm, and the maximum is 170 rpm.

schemes, a validation experiment was conducted, using the same Schroeder multisine input described above, but using a non-parametric system identification method, via the Welch method, using the following general relation:

$$\hat{H}_v(f) = \frac{P_{yu}(f)}{P_{uu}(f)}, \tag{3}$$

with $P_{uy}(f)$ the cross-spectral density and $P_{uu}(f)$ and $P_{yy}(f)$ the auto-spectral density of the input (u) and output (y) signals respectively, by specifying the desired velocity ω_{des} as the input variable and the measured ω as the output variable. The resulting Bode plot, for each of the peak desired velocity values considered, is shown in Fig. 5(e). The feedforward compensation scheme cancels the resonant behavior, without excessively penalizing the inner loop bandwidth at low velocity, which amounts to 15 Hz for the low-velocity range (from 14 rpm to 75 rpm), and decreases to 3.5 Hz for the high-velocity range (higher than 125 rpm).

2) Perturbed motor case: A torque perturbation experiment was conducted to estimate the transfer function $D_V(s)$. In this experiment, a DC motor was current-controlled to apply perturbation torques to the USM motor of the MR-SEA through a transmission stage composed of standard spur gears. With the motor powered off, it was possible to test that the static friction torque of the motor was higher than 0.5 Nm, thus confirming the intrinsic non-backdrivability of the USM, provided by its actuation principle. A further experiment was conducted, when the motor was commanded a constant velocity within its admissible range, and the motor was current-controlled through a symmetric Schroeder multisine profile. In such conditions, the controlled-motor admittance transfer function was estimated through the same method described in (3), but using the applied torque τ_L as the input variable, and the velocity regulation error $\omega_M - \omega_{des}$ as the output variable.

The applied perturbation on the USM motor shaft had amplitude equal to the peak force of interaction of the SEA during operation, with flat frequency content in the range (0.1 - 10) Hz. The Bode plot of the resulting transfer function is shown in Fig. 6(b) for different values of USM commanded velocity. The plot shows that for the considered perturbation torques (0.092 Nm, corresponding to a linear force of 17 N), the resulting change in motor velocity is lower than 1 rpm, 2% of the minimum commanded value.

B. Control

After demonstrating that the velocity-controlled USM has a low intrinsic admittance, we now hypothesize that the term $D_V(s)F_L(s)$ is negligible compared to the first term in (2), implying no effect on the velocity control performance is derived from loading effects. Under the mentioned assumption, the velocity-controlled ultrasonic motor is modeled as the series of a non-linear block, which models motor continuous and intermittent mechanical power limit, and a low-pass filter, which takes into account the time required to change velocity from a current value to a new specified value. The non-linear block implements the following discontinuous function between the input variable v and the output variable $f(v)$:

$$f(v) = \begin{cases} v_{min}\mathrm{sign}(v) & \text{if } |v| < v_{min} \\ v & \text{if } v_{min} < |v| \leq v_{max} \\ v_{max}\mathrm{sign}(v) & \text{if } |v| > v_{max} \end{cases} \tag{4}$$

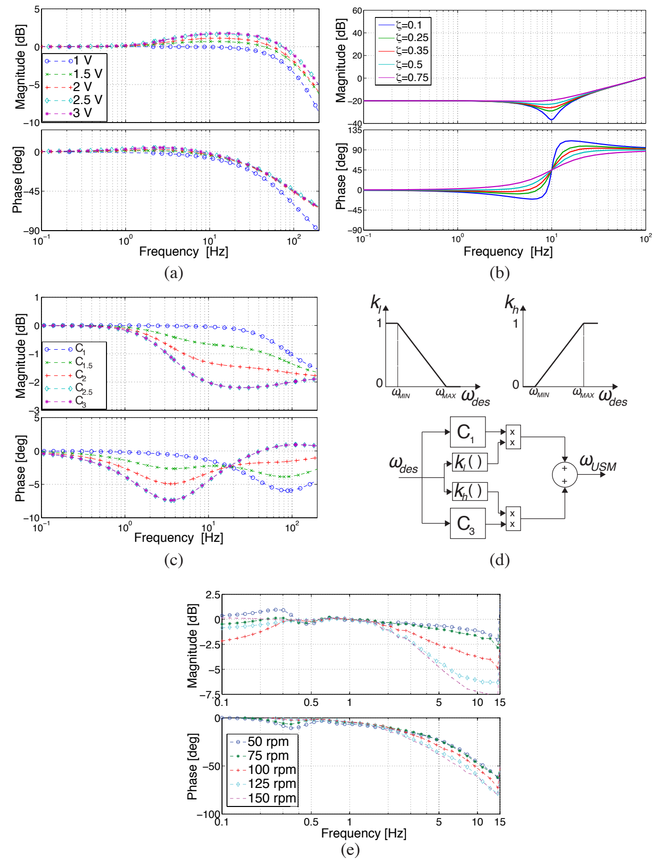

Fig. 5. USM motor amplitude-dependent inner velocity loop compensation. (a) Estimated inner velocity loop transfer function, for different values of peak applied voltage, obtained as a parametric transfer function with two underdamped poles and one zero. (b) Impedance transfer function of a SEA with proportional force control, that employs a resonant inner velocity loop. For a given force control feedback gain, passivity can be compromised if the damping ratio is low. (c) Inversion of the transfer function shown in (a), with fixed poles and zeros and amplitude-dependent ζ. (d) Amplitude-dependent compensation scheme, based on weighting the compensators described above, through the maps $k_l(\omega_{des})$ and $k_h(\omega_{des})$. (e) Experimental estimate of the velocity control transfer function for the compensated system.

Defining the state vector $\mathbf{x} = [x_1, x_2]^T$, with variables $x_1 = (F_L - F_{des})/k_S$ and $x_2 = \dot{x}_M$, in the case of a constant desired force $\dot{F}_{des} = 0$, the state equations of the unperturbed system ($x_L = 0$), subject to feedback control law control $v(x_1)$ can be defined as:

$$\dot{\mathbf{x}} = \mathbf{f}(\mathbf{x}) = \begin{bmatrix} x_2 \\ -\frac{x_2}{T} - \frac{k_S k_{p,f}(x_1)}{T} \end{bmatrix} \quad (5)$$

A detailed stability analysis for the system controlled through the switching controller action is provided in [33], demonstrating the asymptotic stability of the resulting discontinuous dynamical system for force control in blocked output conditions. An extensive simulation-based analysis describes the performance limit of the actuator for both force control in blocked output conditions (8 Hz bandwidth), and for stiffness control, during interaction with an environment described as an ideal velocity source, validating the feasibility of the proposed control action. In the following section, the implemented

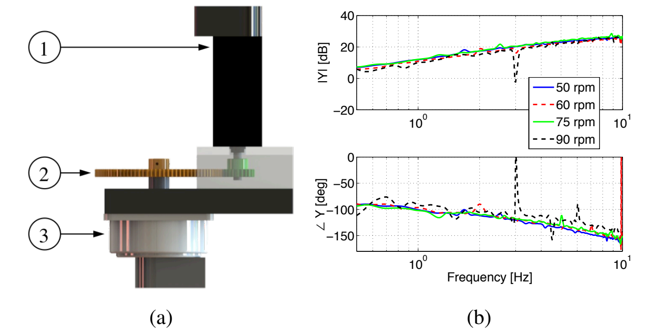

Fig. 6. (a) 3D rendering of the setup used for the perturbation experiments to determine the transfer function $D_V(s)$. (1) DC motor used for perturbation, (2) spur gears (modulus 0.5, reduction ratio 3:1), (3) USM tested. (b) Bode plot of the admittance transfer function under constant velocity command, defined as the change in velocity (in rpm) under torque perturbation $Y = \frac{\omega_M - \omega_{des}}{T_{pert}}$.

controller will be validated in experimental tests performed on the prototype described in Section II-C.

IV. Experimental validation

A. Accuracy of force measurement

Due to the particular mechatronic design of the MR-SEA and to its sensorization, force measurement accuracy is affected by the static friction of the linear bearings and by the slider mass. We conducted a preliminary set of experiments aimed at quantifying the accuracy of force measurement obtained from the deflection of the spring. In the first experiment, the motor was unpowered and an ATI-Nano17 force sensor was connected to the moving slider. With the motor in this configuration, horizontal forces were applied to the platform through the force sensor, resulting in the movement of the slider (but not of the motor, due to its non-backdrivability). In these conditions, neglecting the extensibility of the transmission wire, the load displacement x_L was equal to the springs' deflection, and the force sensor could be used to calibrate the equivalent spring rate and to assess the amount of static friction in the linear bearings when loaded. After calculating the load velocity using a fourth order Savitzky-Golay filter, in a window comprising 51 samples, a multiple linear regression analysis was used to estimate the parameters of a spring-damper system with static friction:

$$F_L = k_S x_L + F_{static}\,\mathrm{sign}(v_L) + b_L v_L; \quad (6)$$

yielding the parameters $k_S = 3.85 \cdot 10^3$ N/m, $F_{static} = 0.55$ N, $|b_L| < 0.1$ Ns/m, with a coefficient of determination $R^2 = 0.997$, and a maximum absolute deviation of 0.90 N.

B. Interaction control capabilities

Having determined the measured force accuracy, the MR-SEA was experimentally evaluated to assess its capability to regulate interaction with a subject, who applied perturbations to the slider. The controller, based on the cascaded force-velocity scheme shown in Fig. 3(c), using the amplitude-dependent inner loop velocity compensation scheme described in Sec. III-A.1, was implemented in Simulink (The MathWorks, Inc.), and was translated into real time code using

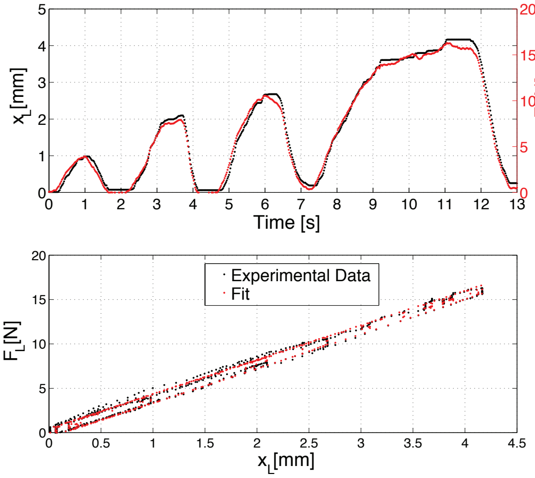

Fig. 7. Calibration of force measurement through springs' deflection. Fitted curve: $F_L = k_S x_L + F_{static}\text{sign}(v_l)$, with $k_S = 3.85 \cdot 10^3$ N/m, $F_{static} = 0.55$ N, $R^2 = 0.997$. For quality of representation, measured points have been downsampled at a 50 Hz frequency.

QuaRC (Quanser Inc.), at a sampling rate of 1 kHz. In all cases, a simple proportional action was used for the force controller, i.e. $C_F(s) = k_{p,f}$. To avoid the switching behavior around the set-point, introduced by the inner velocity loop non-linearity around the zero-desired velocity, a dead-zone non-linearity of 0.19 N was introduced in the measured force signal, and the motor was powered off when the force control error was lower than this threshold[8].

1) Zero force mode: During force control ($F_{des} = 0$) the output impedance Z_S was estimated at the point of interaction with the environment from the spring deflection measurement x_S. $Z_S = \frac{F_S}{v_L}$ has the following theoretical expression, deriving from the linear model presented in Sec. III:

$$Z_S(s) = \frac{k_S + k_S \tau s}{\tau s^2 + s + k_{P,F} k_S} \tag{7}$$

At low frequencies, the transfer function reduces to a damper, with a coefficient inversely proportional to the outer loop gain, $b_{eq} = \frac{1}{k_{p,f}}$. It is then clear that the resulting effect of a proportional controller is that of compensating for motor non-backdrivability, inducing a velocity-dependent resistance force that can be reduced proportionally to the value of the force feedback gain. This controller was implemented in the linear actuator prototype described above, using a gain of 0.12 m/sN for the outer force loop, resulting in a theoretical coefficient of friction of 8.33 Ns/m.

A manual perturbation test was conducted, with a subject applying forces to the platform through a ATI-Nano17 force sensor, moving the platform throughout the actuator workspace, imposing oscillatory movements with frequency comprised between 0.5 Hz and 3 Hz, with a speed comprised between 0 and 0.08 m/s. The methodology of human perturbation was chosen despite its limited repeatability because it is capable of mimicking the range of forces and velocities in the actuated joints' space that reproduce the 2 DOF wrist movements intended with the robot (see Section II for a detailed analysis of specifications).

[8]Due to its actuation principle and intrinsic non-backdrivability, the motor has very fast unpowering dynamics, with the velocity switching to zero in less than 2 ms

TABLE II

PARAMETERS OF THE RENDERED IMPEDANCE DURING ZERO-FORCE MODE

Quantity	Model	b_{eq} [Ns/m]	F_S [N]	m_{eq} [kg]	R^2
Z_S	Analytical	8.33[9]	-	-	-
Z_S	"pem" System ID	14.72	-	-	0.84
Z_S	NL System ID	8.81	0.18	-	0.87
Z_S	Mass-damper	8.81	0.18	0.26	0.89
Z_L	NL model	8.3	0.62	0.30	0.92

The impedance transfer function Z_S was estimated through different system ID techniques. After calculating the load velocity as reported in the previous experiment, the transfer function Z_S was computed through parametric system ID to estimate the coefficients in (7), using the MATLAB function `pem`. A Bode plot of the calculated transfer function is shown in Fig. 8. It can be seen that the transfer function has a flat low-frequency region in which it essentially behaves as a damper with a roughly constant amplitude and zero phase; however the damping coefficient at low frequencies is higher than the value calculated from the model, due to the dead-band introduced in the force control loop that increases the perceived impedance. To better characterize the effect of the outer loop dead-band, a nonlinear system ID analysis was conducted through multiple linear regression, using the following general linear model in the variables v_L and $\text{sign}(v_L)$:

$$F_S = b_L v_L + F_{static}\text{sign}(v_L) \tag{8}$$

where the static friction term F_{static} is defined from the measured velocity profile, using the analytical function $\text{atan}(v_L)$ for smoothing. The results of the nonlinear system ID are reported in Table II, which shows that the estimated coefficient of viscous friction is approximately equal to the coefficient deriving from the linear model analysis (within 5%), and that an additional 0.18 N of static friction are introduced due to the dead-band of the outer force loop. To model the increase in amplitude of the impedance transfer function (7) at higher frequencies, the coefficients of a spring-damper model with static friction were also estimated, using the regressor matrix $X_2 = \begin{bmatrix} v_L & a_S & 1 \end{bmatrix}$, which includes an estimate of the load acceleration. The estimated coefficients obtained through this model are reported in Table II and the estimated transfer function is plotted in Fig. 8.

A further analysis was conducted based on the direct measurement of the interaction force F_L, obtained through the force sensor. In SEAs, F_L will generally be equal to F_S throughout the frequency range of interest. For the MR-SEA, the relation is different, due to non-negligible friction in the linear bearings and platform mass. Through measurement from the force sensor, it was possible to estimate the impedance

[9]Calculated as $1/k_{p,f}$.

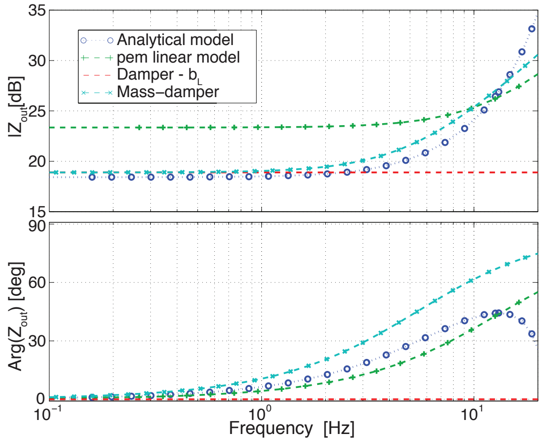

Fig. 8. Bode plot of the impedance transfer function $Z_{out}(s)$, estimated in the zero-force experiments.

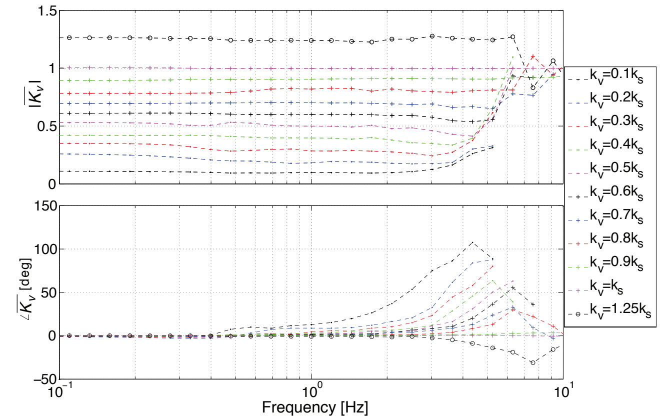

Fig. 9. Bode plot of the normalized virtual stiffness transfer function $\overline{K}_V(s) = \frac{K_V(s)}{k_S}$ estimated during the human perturbation experiment, for different values of desired stiffness k_V commanded to the SEA.

$Z_L = \frac{F_L}{v_L}$ perceived by the user, whose estimate is provided in Table II. It can be seen that the user-reflected impedance has a higher static friction than the one estimated through spring deflection, due to the presence of the non-ideal linear graphite bearings. The 0.44 N increase in static friction is coherent with the measurement performed without the motor connected to the load, demonstrating insensitivity of the bearings' mechanical properties during loading. The inertia reflected during interaction is estimated as 0.3 kg[10].

2) Stiffness control mode: During stiffness control, the system was controlled using the same cascaded force-velocity control scheme shown in Fig. 3(c), but with an outer impedance loop, that specified the desired force F_{des} as a virtual wall with variable stiffness k_V:

$$F_{des} = -k_V(x_L - x_0) \tag{9}$$

During the same experiment, the force feedback gain $C_F = k_{p,f}$ was determined through a linear gain-scheduling algorithm, that defined $k_{p,f}$ as a linear function of the value of desired virtual stiffness for that specific experiment. The extremal points of the mapping were determined by increasing the gain for the conditions $k_V = 0.9k_S$ and $k_V = 0.1k_S$ as long as coupled stability was maintained even during application of a step-like force perturbation with instantaneous release of the slider[11]. The value at the extreme points was obtained as $k_{p,f}|^{0.1k_S} = 0.08$ m/Ns and $k_{p,f}|^{0.9k_S} = 0.04$ m/Ns.

In order to quantify performance obtainable for values of virtual stiffness in the range considered for the application, a characterization experiment was performed. During the experiment, a human subject applied perturbations to the slider, conducting two trials for each value of virtual stiffness considered, in the range [0.1 1.25] k_S, as reported in Fig. 9. During each trial, the subject alternated between the application of continuous, roughly sinusoidal displacements to the slider and the application of impulsive, impact-like displacements. This was done in attempt to excite the system also at frequencies higher than the ones that could be excited through continuous manual perturbation. The same system ID technique described in (3) was followed, this time specifying the position x_L as the input variable, and the measured force F_S as the output variable, thus estimating the stiffness transfer function $K_V(s)$. Through this technique, issues related to the estimate of derivative of quantized signals were avoided. The two transfer functions estimated for each of the experiments conducted at the same value of k_V were resampled in a 51-elements, logarithmically spaced frequency vector, ($[0.01 - 100]$ Hz), and averaged to obtain the resulting transfer function $K_V(s)$, for that specified value of desired virtual stiffness k_V. Only estimates with a sufficient coherence function (i.e. higher than 0.8) were considered in the averaging and in the analysis (i.e. no point is reported in Fig. 9 if neither of the two estimated transfer functions has a sufficient coherence at that frequency).

The resulting estimated transfer functions are reported in Fig. 9. For all values of desired stiffness, it is possible to distinguish two areas. In a low frequency range, the system behaves as a pure spring, and the estimated virtual stiffness value $\hat{k}_V$ matches the corresponding desired value k_V. At higher frequencies, instead, the controlled system reduces itself to displaying the physical stiffness of the spring, reflecting the fact that the inner velocity control loop is not fast enough to compensate for the measured force error. The stiffness control bandwidth can be defined, as in [34], as the frequency at which the ratio between the displayed virtual stiffness and the desired stiffness equals 3dB. The value of the stiffness control bandwidth ranges between 4 Hz (for the lower k_V values) and 8-9 Hz (for the higher k_V values). Through gain scheduling, the bandwidth of stiffness control is improved at low stiffness; stiffness control bandwidth obtained at $k_V = 0.1k_S$, using a fixed-gain controller with gain tuned to ensure coupled

[10]The estimated inertia is higher than the physical mass of the slider, which weighs approximately 80 g. This inertia is mainly resulting from the intrinsic behavior of the zero-force controlled series elastic actuator, that provides increased impedance in the frequency range around its inner velocity control loop pole. Due to the difficulty in exciting the frequencies higher than the inner velocity loop pole, an acceptable fit is obtained through multiple linear regression of a mass-damper model with static friction, see also Fig. 8.

[11]This condition is recognized as being the most destabilizing perturbation in force-feedback controlled systems

stability at high stiffness (using $k_{p,f} = k_{p,f}|^{0.9k_S}$) reduces to 1.5 Hz.

C. MR-compatibility testing

Experiments were conducted to test the MR-compatibility of the MR-SEA during simultaneous operation and scanning. As defined in [35] and in the following literature [4], compatibility refers to the capability of a robotic/mechatronic device to satisfy simultaneously the following conditions: *i)* it is MR safe, *ii)* it is capable of operating as designed in the MR environment, and *iii)* its use in the MR environment does not affect imaging quality.

Addressing point *i)* above, we did not experience any hazardous situations when including the MR-SEA in the scanner (i.e. no magnetic forces applied on the device, no heating of mechanical parts). This is not surprising since the prototype is designed using low-susceptibility and low-conductivity materials (refer to Table I).

1) Capability of operation during MRI: The MR-SEA was then tested inside a Philips Ingenia 3T scanner, that employed a 32-element SENSE coil loaded with a Radio-Frequency (RF) phantom filled with a saline water solution. The USM motor axis was placed so to replicate the conditions during operation of the closest of the actuators of the wrist exoskeleton described in Section II. Experiments were conducted in different conditions. In the first condition, the scanner was not collecting images and the RF coil was turned off (RF off); while in the second condition, the coil was powered according to a T2*-weighted gradient echo-planar imaging sequence (RF on), used for functional neuroimaging studies (sequence details are in Table III). The MR-SEA was commanded to track a sinusoidal trajectory (amplitude 8 mm, frequency 0.5 Hz), closing a proportional position feedback loop on the load measurement. The resulting trajectory during operation inside the scanner was indistinguishable from the one acquired outside the scanner room, (maximum error in the acquired trajectories is within 0.5 mm in all cases).

2) Effect on imaging quality: To further address the effect introduced by the presence and the movement of the actuator during scanning, image quality was assessed using the NEMA standards, for both Signal-to-Noise Ratio [36], and spatial homogeneity [37]. Both measures were computed during three different scanning protocols: *i)* functional imaging T2*-weighted gradient echo-planar sequence, *ii)* T1-weighted gradient echo, and *iii)* T2-weghted spin dual echo, and under different experimental conditions: *a)* with the device out of the scanner (baseline), *b)* with the device inside the scanner, but unpowered, and *c)* with the device inside the scanner and moving as described above. In order to verify repeatability of the measures and their insensitivity to the low frequency thermal drift of the scanner, condition *a)* was repeated at the end of the experiment.

Signal-to-Noise Ratio (SNR) is a general measure used by scanner manufacturers to define the quality of scanned images. This measure is heavily used also in the field of MR-compatible robotics to assess MR-compatibility of devices. For quantification of SNR, we followed the guidelines in [37] and used method 4, due to its inherent robustness to the low frequency drift of magnetic excitation during MRI. This measure involves the definition of an ROI in the center of the phantom, which covers at least 85% of the phantom area. The signal $\bar{S}$ is calculated as the average value of the pixel intensities within the ROI. The measurement of noise is calculated from the same image, but using the pixel intensities in four rectangular areas in the background of the image, including at least 1000 pixels for robustness. Within this area, the noise is calculated from the standard deviation of the measured signal intensity, using a correction factor of 0.66 to account for the non-normal distribution of the scanned images [37].

Although it was not considered in previous studies addressing MR-compatibility of mechatronic devices, spatial homogeneity is also an important measure to define quality of MRI images. Spatial homogeneity is especially relevant to the field of MR-compatible mechatronics, since it is sensitive to spatial inhomogeneities potentially introduced in the ROI by interfering objects or signals. In contrast, the SNR measure only involves measurement of the ratio between the value of average signal measured within the ROI and the noise measured outside the ROI, and is much less sensitive to spatial changes in the signal within the ROI. Two measures of spatial inhomogeneities are defined in the NEMA standard, the Peak Deviation Non-Uniformity (PDNU), and the Normalized Absolute Average Deviation Uniformity (NAADU). For computation of PDNU, the image is first filtered using a nine-point low pass filter to smooth the pixel intensities. After computing the maximum (S_{max}) and minimum (S_{min}) values of pixel intensity within the ROI, PDNU is computed as:

$$\mathrm{PDNU} = 100\frac{S_{max} - S_{min}}{S_{max} + S_{min}}. \tag{10}$$

NAADU is defined as the non-squared sum of residuals of the intensities of the n pixels within the ROI, as

$$\mathrm{NAADU} = 100\left(1 - \frac{1}{n\bar{S}}\right)\sum_{i=1}^{n}\left|S_i - \bar{S}\right|. \tag{11}$$

For each scanning protocol and each experimental condition, SNR, PDNU and NAADU were computed in eleven slices aligned with those of structural scans, as described in Table III. The distribution of the calculated indices is reported in the box plots in Fig. 10. The measured distributions were subject to statistical analysis to evaluate the significance of the effect "experimental condition" for each of the scanning sequences. Given the weak normality of the measured distributions, statistical inference was conducted through separate non-parametric Kruskal-Wallis tests, for each scanning protocol, for each measure of interest, to test the null hypothesis stating that the mean rank of samples for the given measure of interest, in each experimental condition, is the same. The effect of the experimental condition was not significant at the $p < 0.05$ significance level for each image quality index and for each scanning protocol, as detailed in the p-values table, Table IV.

Through the statistical analysis, we demonstrate that neither the presence nor the movement of the actuator in the scanner, significantly degrade the quality of acquired images, thereby proving the MR-compatibility of the MR-SEA.

TABLE III
SEQUENCES USED FOR MR-COMPATIBILITY TESTING

Sequence	Voxel Size [mm]	Image size [px]	TE [ms]	TR [ms]	Flip angle [deg]	Number of slices
Gradient-echo planar (fMRI)	1.56x1.56x3	160x160	35	3000	90	35
T1 weighted	0.976x0.976x5	256x256	20	500	90	11
T2* weighted dual echo	0.976x0.976x5	256x256	16, 80	2000	90	11

V. Discussion and Conclusions

This paper demonstrates the possibilities of interaction control of a novel compliant, force-feedback actuator, the MR-SEA, designed for a parallel wrist exoskeleton for motor protocols during continuous fMRI. The main result of this paper is the demonstration of the capability of displaying through control both a low-impedance, subject-in-charge mode, and a high-impedance mode, in which the robot applies elastic force fields towards a desired kinematic status. Further, experiments in a 3 T scanner demonstrate the possibility of simultaneous actuation and scanning of the force-controlled actuator.

The paper presents a detailed analysis of specifications for the case of a MR-compatible wrist robot design, that results in the list of requirements for the linear actuator that is described hereafter. The actuator, purposively developed within the defined specifications, has a novel design, resulting from the inclusion of a cable transmission and preloaded extension springs in series between a rotary piezoelectric motor and the load, that paraphrases the SEA architecture to the specific needs of interaction control in MR environments.

The use of a cable transmission in low-impedance haptic manipulators is not novel, as it has been previously developed in [21] for uncompensated impedance control and in [23] for compliant force-feedback control. The presented solution consists of a novel arrangement of elements for a linear SEA, resulting from the need of minimizing the number of bearings in the system. The use of piezoelectric ultrasonic motors (USM) is well documented in the literature of MR-compatible surgical robots [4], [10]. Preliminary attempts to include one of the actuators in an admittance-controlled system with force feedback [38] and through an ER clutch [39] were reported, but, to the best of our knowledge, no dynamic experiments were presented to describe the impedance control capabilities of the MR-compatible devices. Motivations for the limited inclusion of USMs in admittance control schemes were later indicated in the fact that the velocity control non-linearity of the USM motors impeded the display of accurate forces through force feedback.

In the MR-SEA, achievement of accurate impedance regulation is obtained through inner-loop velocity compensation,

TABLE IV
p-VALUES FOR THE KRUSKAL-WALLIS TESTS, FOR EACH IMAGE QUALITY MEASURE AND SCANNING SEQUENCE

	fMRI	T1	T2a	T2b
SNR	0.12	0.944	0.637	0.9971
PDNU	0.7384	0.3681	0.1999	0.1082
NAADU	0.9661	0.777	0.3523	0.3763

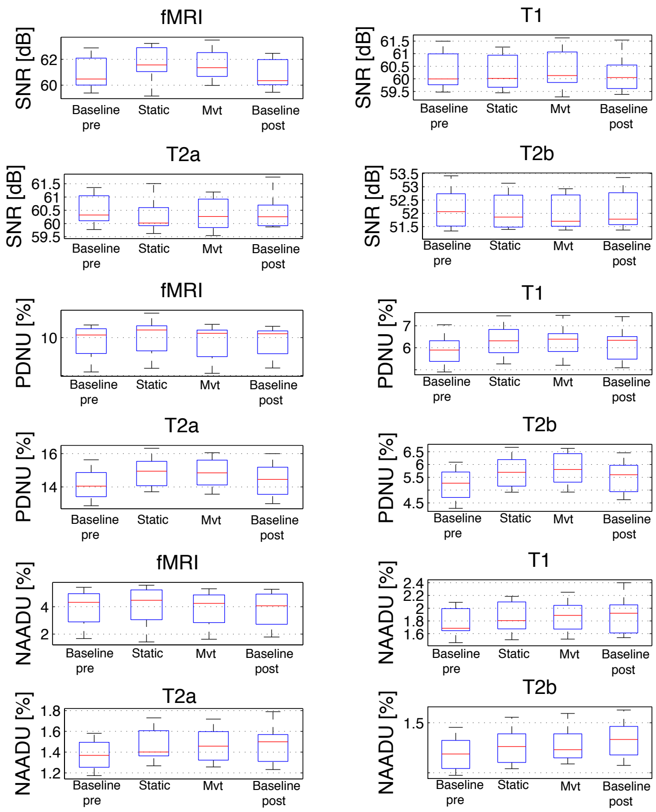

Fig. 10. Measures of image quality in different experimental conditions, for each scanning sequence considered. SNR: signal to noise ratio, in dB units, PDNU: peak deviation non-uniformity, NAADU: normalized absolute average deviation uniformity. Baseline: no device in the scanner. Static: device in the scanner, actuation and signal cables connected to the computer in the control room, device unpowered and stationary. Mvt: device moving through a sinusoidal load position profile, 16 mm peak-to-peak amplitude, frequency: 0.5 Hz. The two images acquired during the dual-echo T2-weighted sequence have been analyzed separately, and labeled as T2a (short echo) and T2b (long echo). The red line indicates the distribution median, the box edges represent the 25^{th} and 75^{th} percentiles, the whiskers extend to the most extreme data points.

and through the inclusion of compliance in series between the actuator and the load. The springs included in this design act as a low-pass filter that decouples the high-frequency switching actions and the non-linearities of the velocity source from the output. Through this novel system, and using a simple cascaded force-velocity control, we demonstrate the ability to accurately render variable levels of impedance in a frequency range compatible with human movements (up to 4 Hz for the worst case considered in the analysis). Force regulation capabilities have not been characterized experimentally in this prototype; however, the demonstration of stiffness control bandwidth greater than 4 Hz outperforms the below-1Hz outer position loop regulation capabilities presented in fully MR-compatible pneumatic and/or hydrodynamic actuation systems described in [7]. Other MR-compatible force source devices were not characterized for force control capabilities and instead mainly used to provide "all-or-none" force perturbations [13].

Two measures were chosen to define the quality of interaction control. The first measure considered is the zero-force dynamic range, defined as the ratio between the maximum value of force that can be displayed to the subject, and the minimum force required to back-drive the robot in the minimum impedance, or zero-force mode. This measure is especially useful when analyzing the behavior of a force-feedback controlled system during the *subject-in-charge* mode. During this phase, especially at the low speeds involved during upper extremity movements, the dynamics of a robot are often dominated by velocity-independent variables, such as static friction, and not by viscous friction, making the velocity-dependent assumption required for the definition of a linear impedance not appropriate. Through the zero-force characterization experiment, we demonstrated that the maximum back-drivability forces when the subject was moving at the maximum selected speeds amounted to less than 1.5 N (considering the static friction of 0.62 N and the viscous friction coefficient of 8.33 Ns/m, with a maximum velocity of 10 cm/s). The maximum backdrivability force in actuator space is mapped in the end-effector space as a maximum backdrivability torque of 0.17 Nm, resulting in a transparent actuator, with a dynamic zero-force range of 23 dB that is in the lower range of wrist rehabilitation robots, as discussed in Sec. II-A. 35% of the maximum back-driving force calculated results from the static friction of the custom bearing. Using an ideal bearing without static friction, the resulting theoretical maximum dynamic zero-force range amounts to 27 dB, similar to the 30 dB reported in [22] outside the MR scanner.

The second measure considered is the range of stiffness values that can be rendered through control of the compliant actuator. Through gain scheduling, we demonstrate the accurate rendering of variable stiffness values, from 10% of the physical actuator stiffness (k_S) to 25% higher than k_S, resulting in a stiffness range of 22 dB, for frequencies up to 4 Hz. As in all stiffness-controlled SEAs, at frequencies above the controller bandwidth, the reflected impedance is dominated by the spring stiffness, hence setting an upper bound to the maximum impedance that can be transferred to the subject during operation. Although through the pursued approach (inclusion of compliance and use of a cascaded force-velocity controller) it is difficult to render high-stiffness virtual walls (i.e. with virtual stiffness in the order of 50 N/mm), the possibility of stably displaying walls with virtual stiffness higher than the physical stiffness of the spring is demonstrated in this paper. Stability at higher values of stiffness could be improved through impedance compensation with an explicit introduction of damping in the system. Such approaches are possible in SEAs when using high-impedance, velocity-sourced actuators, as discussed in a companion paper [40].

The final result presented in the paper demonstrates the MR-compatibility of the MR-SEA, and is in agreement with the previously demonstrated compatibility of the selected USM motor [38], while in disagreement with [11]. The problem of MR-compatibility of mechatronic systems is complex and it is not easy to indicate which specific measure was responsible for the obtained compatibility. Differently from what presented in [11], we used shielded cables for both motor power and encoder signals, and used capacitive low-pass filtering on the encoder lines to remove noise in the MHz region. Other factors of influence reside in the control box of the actuator, improved in recent years, that was placed outside the scanning room through shielded lines. Finally, it is important to note that MR-compatibility was proven only for the specific experimental arrangement tested, defined also by the relative location of the motor in the scanner. Such location was specified considering where actuators are to be placed when included in the parallel robot shown in Fig. 1. Given the presence of metallic moving parts and of electrical signals, it is possible that degradation in the considered MR-compatibility measures can occur, when the actuator is placed closer to the ROI.

VI. ACKNOWLEDGMENT

The authors would like to thank Dr. Jeff Anderson and Dr. Christoph Karmonik from the Methodist Hospital Research Institute for their support in the definition of the scanning sequences and protocols used in this work. This research was supported in part by a TIRR Memorial Hermann Pilot grant, by the H133P0800007-NIDRR-ARRT fellowship, by the NSF GRFP 0940902, and by the NSF CNS-1135916.

REFERENCES

[1] N. Hogan, H. I. Krebs, B. Rohrer *et al.*, "Motions or muscles? Some behavioral factors underlying robotic assistance of motor recovery," *The Journal of Rehabilitation Research and Development*, vol. 43, no. 5, p. 605, 2006.

[2] A. R. Carter, L. T. Connor, and A. W. Dromerick, "Rehabilitation After Stroke: Current State of the Science," *Current Neurology and Neuroscience Reports*, vol. 10, no. 3, pp. 158–166, Mar. 2010.

[3] J. F. Schenck, "The role of magnetic susceptibility in magnetic resonance imaging: MRI magnetic compatibility of the first and second kinds." *Medical Physics*, vol. 23, no. 6, pp. 815–850, 1996.

[4] H. Elhawary, Z. T. H. Tse, A. Hamed *et al.*, "The case for MR-compatible robotics: a review of the state of the art." *International Journal of Medical Robotics*, vol. 4, no. 2, pp. 105–113, May 2008.

[5] S. Menon, G. Brantner, C. Aholt *et al.*, "Haptic fMRI : Combining Functional Neuroimaging with Haptics for Studying the Brain's Motor Control Representation," in *35th Annual International IEEE EMBS Conference, July 3-7, 2013, Osaka International Convention Center, in Osaka, Japan*, Jul. 2013, pp. 1–6.

[6] R. Gassert, R. Moser, E. Burdet *et al.*, "MRI/fMRI-Compatible Robotic System With Force Feedback for Interaction With Human Motion," *IEEE/ASME Transactions on Mechatronics*, vol. 11, no. 2, pp. 216–224, Mar. 2006.

[7] N. Yu, C. Hollnagel, A. Blickenstorfer *et al.*, "Comparison of MRI-Compatible Mechatronic Systems With Hydrodynamic and Pneumatic Actuation," *IEEE/ASME Transactions on Mechatronics*, vol. 13, no. 3, pp. 268–277, May 2008.

[8] A. Khanicheh, D. Mintzopoulos, B. Weinberg *et al.*, "MR-CHIROD v.2: Magnetic Resonance Compatible Smart Hand Rehabilitation Device for Brain Imaging," *IEEE Transactions on Neural Systems and Rehabilitation Engineering*, vol. 16, no. 1, pp. 91–98, 2008.

[9] O. Unluhisarcikli, B. Weinberg, M. Sivak *et al.*, "A robotic hand rehabilitation system with interactive gaming using novel Electro-Rheological Fluid based actuators," *Robotics and Automation (ICRA), 2010 IEEE International Conference on*, pp. 1846–1851, 2010.

[10] K. Chinzei, N. Hata, F. Jolesz *et al.*, "MR Compatible Surgical Assist Robot: System Integration and Preliminary Feasibility Study," *Proc. Med. Image Comput. Comput.-Assisted Intervention*, pp. 921–30, Jul. 2000.

[11] G. Fischer, "MRI compatibility of robot actuation techniques–a comparative study," *Medical Image Computing Computed Assisted Intervenation*, 2008.

[12] N. Hogan and S. P. Buerger, "Interaction Control." CRC Handbook on Robotics and Automation, Aug. 2005, pp. 1–24.

[13] J. Diedrichsen, Y. Hashambhoy, T. Rane *et al.*, "Neural correlates of reach errors," *J Neurosci*, vol. 25, no. 43, pp. 9919–9931, Sep. 2005.

[14] Sergi, F. Krebs, H. I. Groisser *et al.*, "Predicting Efficacy of Robot-Aided Rehabilitation in Chronic Stroke Patients Using an MRI-Compatible Robotic Device," *Proceedings of the International IEEE EMBS Conference*, pp. 7470–7473, Jun. 2011.

[15] R. Gassert, L. Dovat, O. Lambercy *et al.*, "A 2-DOF fMRI Compatible Haptic Interface to Investigate the Neural Control of Arm Movements," in *Proceedings of the 2006 IEEE International Conference on Robotics and Automation*, Apr. 2006, pp. 3825–3831.

[16] N. Yu, N. Estévez, M. C. Hepp-Reymond *et al.*, "fMRI assessment of upper extremity related brain activation with an MRI-compatible manipulandum," *International Journal of Computer Assisted Radiology and Surgery*, Aug. 2010.

[17] R. M. Birn, R. W. Cox, and P. A. Bandettini, "Experimental designs and processing strategies for fMRI studies involving overt verbal responses," *NeuroImage*, vol. 23, no. 3, pp. 1046–1058, Nov. 2004.

[18] T. Lemmin, G. Ganesh, R. Gassert *et al.*, "Model-based attenuation of movement artifacts in fMRI," *Journal of neuroscience methods*, vol. 192, no. 1, pp. 58–69, Sep. 2010.

[19] M. M. Williamson, "Series Elastic Actuators," *PhD thesis, MIT*, pp. 1–83, 1995.

[20] J. Rosen, J. C. Perry, N. Manning *et al.*, "The human arm kinematics and dynamics during daily activities-toward a 7 DOF upper limb powered exoskeleton," *Advanced Robotics, 2005. ICAR'05. Proceedings.*, pp. 532–539, 2005.

[21] A. Gupta, M. K. O'Malley, V. Patoglu *et al.*, "Design, Control and Performance of RiceWrist: A Force Feedback Wrist Exoskeleton for Rehabilitation and Training," *The International Journal of Robotics Research*, vol. 27, no. 2, pp. 233–251, Feb. 2008.

[22] H. I. Krebs, B. T. Volpe, D. Williams *et al.*, "Robot-Aided Neurorehabilitation: A Robot for Wrist Rehabilitation," *IEEE Transactions on Neural Systems and Rehabilitation Engineering*, vol. 15, no. 3, pp. 327–335, Dec. 2007.

[23] F. Sergi, M. M. Lee, and M. K. O'Malley, "Design of a series elastic actuator for a compliant parallel wrist rehabilitation robot," in *2013 IEEE International Conference on Rehabilitation Robotics*, Seattle, WA, USA, Jun. 2013, pp. 1–6.

[24] L. Masia, M. Casadio, P. Giannoni *et al.*, "Performance adaptive training control strategy for recovering wrist movements in stroke patients: a preliminary, feasibility study," *Journal of NeuroEngineering and Rehabilitation*, vol. 6, no. 1, p. 44, 2009.

[25] A. U. Pehlivan, F. Sergi, A. Erwin *et al.*, "Design and Validation of the RiceWrist-S Exoskeleton for Robotic Rehabilitation After Incomplete Spinal Cord Injury," *Robotica*, vol. 32, no. 8, pp.1415-1431, 2014.

[26] D. Formica, S. K. Charles, L. Zollo *et al.*, "The Passive Stiffness of the Wrist and Forearm," *Journal of neurophysiology*, vol. 108, no. 4, pp. 1158–1166, Aug. 2012.

[27] L. Masia, M. Casadio, G. Sandini *et al.*, "Eye-Hand Coordination during Dynamic Visuomotor Rotations," *PLoS ONE*, vol. 4, no. 9, p. e7004, 2009.

[28] G. A. Pratt, M. M. Williamson, P. Dillworth *et al.*, "Stiffness isn't everything," in *Fourth International Symposium on Experimental Robotics*, Jan. 1995, pp. 1–6.

[29] K. Kong, J. Bae, and M. Tomizuka, "A Compact Rotary Series Elastic Actuator for Human Assistive Systems," *IEEE/ASME Transactions on Mechatronics*, vol. 17, no. 2, pp. 288–297, Feb. 2012.

[30] J. W. Sensinger, "Improvements to series elastic actuators," in *Mechatronic and Embedded Systems and Applications, Proceedings of the 2nd IEEE/ASME International Conference on*. IEEE, 2006, pp. 1–7.

[31] G. F. Wyeth, "Control issues for velocity sourced Series Elastic Actuators," *Proceedings of the Australasian Conference on Robotics and Automation*, Dec. 2006.

[32] H. Vallery, J. Veneman, E. van Asseldonk *et al.*, "Compliant actuation of rehabilitation robots," *Robotics & Automation Magazine, IEEE*, vol. 15, no. 3, pp. 60–69, Jan. 2008.

[33] F. Sergi, V. Chawda, and M. K. O'Malley, "Interaction control of a non-backdriveable MR-compatible actuator through series elasticity," in *Proceedings of the 6th Annual ASME Dynamic Systems and Controls Conference, Palo Alto, CA, October 21-23.*, Oct. 2013.

[34] F. Sergi, D. Accoto, G. Carpino *et al.*, "Design and characterization of a compact rotary Series Elastic Actuator for knee assistance during overground walking," *Biomedical Robotics and Biomechatronics (BioRob), 2012 4th IEEE RAS & EMBS International Conference on*, pp. 1931–1936, 2012.

[35] K. Chinzei, R. Kikinis, and F. A. Jolesz, "MR Compatibility of Mechatronic Devices: Design Criteria," *Lecture Notes in Computer Science*, vol. 1679, pp. 1020–1030, 1999.

[36] National Electrical Manufacturers Association, "NEMA Standards Publication MS 1-2008, *Determination of Signal-to-Noise Ratio (SNR) in Diagnostic Magnetic Resonance Imaging* ," 2008.

[37] ——, "NEMA Standards Publication MS 3-2008, *Determination of Image Uniformity in Diagnostic Magnetic Resonance Images*," 2008.

[38] M. Flueckiger, M. Bullo, D. Chapuis *et al.*, "fMRI compatible haptic interface actuated with traveling wave ultrasonic motor," in *Industry Applications Conference, 2005. Fourtieth IAS Annual Meeting. Conference Record of the 2005*, 2005, pp. 2075–2082.

[39] D. Chapuis, R. Gassert, E. Burdet *et al.*, "A hybrid ultrasonic motor and electrorheological fluid clutch actuator for force-feedback in MRI/fMRI," in *30th Annual International IEEE EMBS Conference, August 20-24, 2008*. IEEE, Jul. 2008, pp. 3438–3442.

[40] F. Sergi and M. K. O'Malley, "On the stability and accuracy of high stiffness rendering in non-backdriveable actuators through series elasticity," *Under revision, Mechatronics*, Oct. 2014.

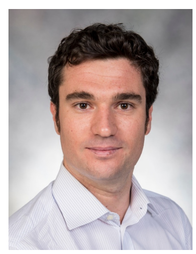

Fabrizio Sergi (M'13) received the B.S, M.S. and Ph.D. degrees in biomedical engineering from Università Campus Bio-Medico di Roma, Rome, Italy, in 2005, 2007 and 2011, respectively. He is currently a Research Scientist in the Department of Mechanical Engineering, Rice University, Houston, TX, USA. His main research interests include wearable robotics, robot-aided neurorehabilitation, and human motor control. He is member of the IEEE, of the IEEE RAS and EMBS societies, and of the ASME.

Andrew Erwin (S'12) received the B.S. degree in mechanical engineering from the University of Massachusetts, Amherst, MA, USA, in 2012, and the M.S. degree in mechanical engineering from Rice University, Houston, TX, USA, in 2014. Supported by an NSF Graduate Research Fellowship, he is currently working toward the Ph.D. degree at the Rice University Mechanical Engineering Department as a member of the Mechatronics and Haptic Interfaces Laboratory. His research interests include MR-compatible robotics, haptics, and mechatronics.

Marcia K. O'Malley (SM'13) is Professor of Mechanical Engineering and of Computer Science, Rice University, Houston, TX, USA, and directs the Mechatronics and Haptic Interfaces Laboratory. She is adjunct faculty in the Departments of Physical Medicine and Rehabilitation at Baylor College of Medicine and the University of Texas Medical School at Houston, and is Director of Rehabilitation Engineering at TIRR-Memorial Hermann Hospital. Her research addresses issues that arise when humans physically interact with robotic systems, with a focus on training and rehabilitation in virtual environments. She is a Fellow of the American Society of Mechanical Engineers and serves as an Associate Editor for the ASME Journal of Mechanisms and Robotics.